Low-energy modification of the γ strength function of the odd-even nucleus ^{115}In

Maud Versteegen,[1,*] David Denis-Petit,[2,1] Vincent Méot,[2] Thomas Bonnet,[1,2] Maxime Comet,[1,2] Franck Gobet,[1] Fazia Hannachi,[1] Medhi Tarisien,[1] Pascal Morel,[2] Marco Martini,[3] and Sophie Péru[2]

[1]*Université de Bordeaux, CNRS-IN2P3, CENBG F-33175 Gradignan, France*

[2]*CEA, DAM/DIF, F-91297 Arpajon, France*

[3]*CEA, DSM/IRFU/SPhN/ESNT, F-91191 Gif sur Yvette Cedex, France*

(Received 27 January 2016; revised manuscript received 24 May 2016; published 28 October 2016)

Photoactivation yield measurements on ^{115}In have been performed at the ELSA facility with Bremsstrahlung photon beams over a range of endpoint energies between 4.5 and 18 MeV. The measured photoexcitation yields of the ^{115m}In metastable state are compared with calculated yields using cross sections obtained with different models of the photon strength function. It is shown that additional photon strength with respect to the general Lorentzian model is needed at 8.1 MeV for the calculated yields to reproduce the data. The origin of this extra strength is unclear, because it is compatible with additional strength predicted in both $E1$ and $M1$ photon strength distributions by quasiparticle random-phase approximation calculations using the Gogny D1S force.

DOI: 10.1103/PhysRevC.94.044325

I. INTRODUCTION

The photon strength function (PSF), along with nuclear level densities, is one of the main ingredients in the calculation of nuclear reaction rates within the statistical model. It is defined via the expected value of the partial radiation width of a γ transition between two levels and can be interpreted as an average reduced γ-transition probability per unit energy.

In the context of astrophysical neutron capture rate evaluations, it has been shown that the low-energy part of the PSF can greatly impact stellar rates [1–4]. Much attention has thus recently been paid to the understanding of additional low-energy resonances in the PSF, observed sitting around the neutron emission threshold energy on the low-energy tail of the giant dipole resonance (GDR). Several studies have reported pygmy dipole resonances (PDR) in the $E1$ dipole strength of a number of neutron-rich nuclei, as reviewed in Ref. [5] and references therein. Magnetic dipole resonances have also been reported at 9 MeV in three isotopes of the zirconium isotopic chain [6].

Systematic experimental studies on the Cd and Sn isotopic chains have shown PDRs at energies between 6 and 9 MeV for ^{105,106,111,112}Cd [7], $^{116-119}$Sn [8], ^{121,122}Sn [9], and ^{116,124}Sn [10]. The results on Cd, $^{116-119}$Sn and ^{121,122}Sn are obtained from (^{3}He ,^{3}He$'\gamma$) and (^{3}He ,$\alpha\gamma$) reactions using the Oslo method [11], whereas the results on ^{116,124}Sn are obtained from high-resolution nuclear resonance fluorescence (NRF) data. The latter allow the determination of absolute values of the PSF at energies below the neutron emission threshold. In these experiments, the measured peak area of a γ line in the NRF spectrum is proportional to the energy-integrated cross section for the excitation of the final state from the ground state, as described in Refs. [5,12,13]. The integrated cross section can be written as a function of the partial decay width to the ground state, usually noted Γ_0, which is proportional to the reduced transition probabilities of all different possible electromagnetic natures. The PSF of each transition character is the average value of the corresponding reduced transition probability. The ^{115}In ($Z = 49$) nucleus is a good candidate to further investigate the PDRs in the Cd ($Z = 48$) and Sn ($Z = 50$) mass regions. It presents a low-energy (∼336 keV), long-lived ($T_{1/2} \sim 4.5$ h) isomer that can be populated by photoexcitation, the activation of which thus strongly depends on the PSF.

Experimental data on the ^{115m}In photoexcitation cross section are surprisingly scarce and contradictory. Early studies show a peak-shaped cross section, with a maximum of a few millibarns at about 8–10 MeV, but disagree on the exact value of the maximum as well as on its position [14,15]. A renewed interest in photoactivation experiments on isomers led to several studies on ^{115}In [13,16,17], but contradictory results about a second maximum at 22 MeV, close to the GDR, have been reported [18,19]. A recent revisitation of these results concluded that no second sharp peak was to be expected at high energies in the cross section [20]. Finally, an effective integrated cross section ($\sigma\Gamma$) is introduced in Ref. [13], with values given at 4 and 6 MeV to be 18 mb keV and 67 mb keV, respectively.

To investigate the possibility of enhanced photon strength in the ^{115}In nucleus, and add new constraints on the photoexcitation cross section of ^{115m}In, new photoactivation data were gathered at the ELSA electron linac of CEA/DAM in Arpajon, France [21]. The measured photoexcitation yields are compared to calculated yields using cross sections obtained with different models of the PSF. The experiment setup and data analysis are described in Secs. II. and III. Section IV presents the calculations of the ^{115}In$(\gamma,\gamma')^{115m}$In cross section and the comparison between simulated and measured yields. It is shown that additional strength with respect to the generalized Lorentzian (GLO) model is needed at 8.1 MeV to reproduce the data, the electromagnetic nature of which is discussed based on microscopic calculations performed within the quasiparticle random-phase approximation (QRPA) approach. Conclusions and perspectives of this work are presented in Sec. V.

*maud.versteegen@cenbg.in2p3.fr

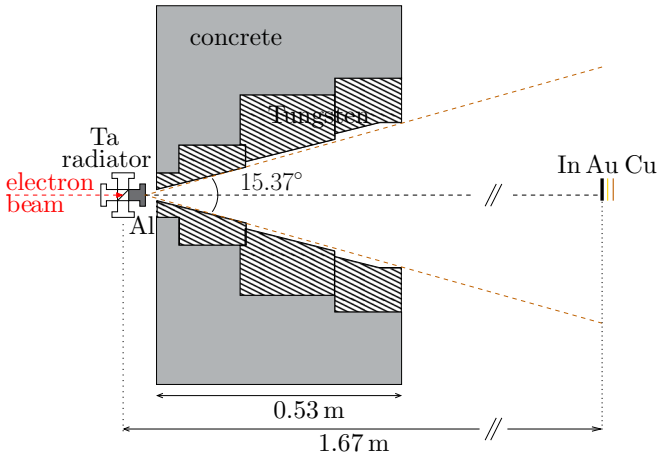

FIG. 1. Experimental setup at ELSA.

II. EXPERIMENTAL SETUP

The monoenergetic electron beam of the radio-frequency electron linac ELSA is obtained by photoinjection, with a 532-nm laser impinging on a Cs_3Sb photocathode. Electron beam energies up to 19 MeV can be reached with very low dispersion (0.05% rms) using four RF cavities. For our purposes, beam intensities between 1.6 and 3.3 μA were set depending on beam energies, which varied between 4.5 and 18 MeV.

As presented in Fig. 1, the electron beam is focused onto a mm-thick tantalum radiator with an angle of incidence of 45° to produce Bremsstrahlung photons. A cylindrical aluminum hardener 40 mm in length is placed against the radiator to absorb low-energy photons as well as high-energy electrons passing through the radiator. The photon beam is then collimated by four cone-shaped collimators mainly composed of tungsten and embedded in the 0.53-m-thick concrete wall separating the accelerator cave from the experimental area. The resulting opening angle of the photon beam is about 15°.

Natural indium, gold, and copper targets were irradiated simultaneously at 1.67 m from the radiator, during 20 min to 2 h depending on beam energy. The gold and copper targets serve as references for the determination of the photon flux. All three targets were replaced between each irradiation by new ones. Radioisotopes and isomeric states with long half lives, as long as 6 days in the case of ^{196}Au, were indeed produced and needed to decay back to the ground state before the target could be irradiated again. Several targets of In, Au, and Cu were thus available. They were disk-shaped, 2.5 cm in diameter. The natural In (95.71% of ^{115}In and 4.29% of ^{113}In) targets were 3 mm thick, with typical masses of 11 g, while the ^{197}Au and natural Cu (69.15% of ^{63}Cu and 30.85% of ^{65}Cu) were 0.1 mm thick, with typical masses of 0.9 and 0.4 g, respectively.

The number of activated nuclei produced during the irradiation was determined offline. The γ spectra of the activated In and Au samples were each measured with a dedicated high-purity germanium (HPGe) detector. Two counting stations were set up, each with one of the HPGe detectors protected from ambient radioactivity by an 11-cm-thick shielding, composed of 10 cm of Pb and 1 cm of Cu. The relative efficiencies of the two HPGe detectors were 80% and 85%. Irradiated In targets were placed at a distance of 6.5 cm from the detector entrance window for counting, and the Au targets were placed at 15.1 cm. The acquisition dead time was under 0.1% and is neglected in the following analysis.

The β^+ activities of the Cu targets corresponding to the ^{64}Cu and ^{62}Cu daughter nuclei of the $^{\text{nat}}$Cu(γ,n) reactions were measured using the multidetector NATALIE [22]. The two 511-keV annihilation photons were detected in coincidence by two NaI detectors, with an efficiency of $5.6 \pm 0.2\%$ or $5.9 \pm 0.2\%$ for ^{62}Cu or ^{64}Cu, respectively. The two radioactive isotopes were identified in the time decay spectrum by their half-lives, equal to 762.06(2) min for ^{64}Cu and 9.673(8) min for ^{62}Cu.

III. DATA ANALYSIS

The data analysis described in the following is split into five parts:

(a) description of the measured γ decay spectrum of In,
(b) determination method of photoactivation yields,
(c) determination of the photon distributions at the scattering site,
(d) determination of neutron production yields, and
(e) determination of the ^{115m}In photoexcitation yields.

A. Measured In decay spectrum

Figure 2 shows a typical offline decay spectrum of an In sample irradiated at the electron beam energy $E_e = 17$ MeV. The 336.2-keV and 391.7-keV γ rays correspond to the deexcitation of the ^{115m}In and ^{113m}In isomers, populated by (γ,γ') and (n,n') processes. The energy, multipolarity, and absolute intensity of the γ rays are presented in the partial level schemes of ^{115}In and ^{113}In in Fig. 3.

The ^{115}In(γ,n) reaction produces the unstable ^{114gs}In, with a lifetime of 71.9 s, and the first isomeric state ^{114m}In, at 190.27 keV, with a lifetime of 49.51 days (see Fig. 4). The ^{114gs}In mainly decays to the ^{114gs}Sn by β^- decay, but a small fraction (0.5% [25]) can also decay by electron capture or β^+

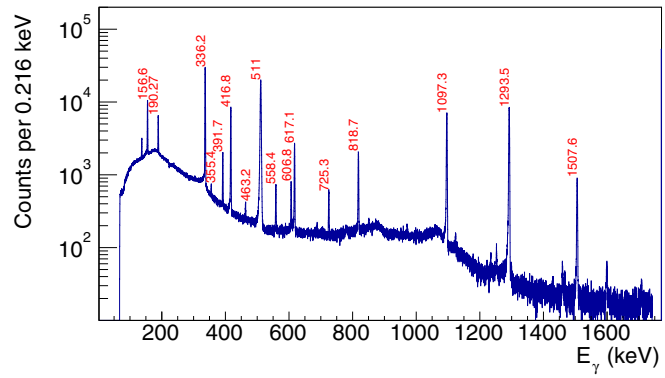

FIG. 2. Measured γ-ray spectrum of an activated natural In sample at $E_e = 17$ MeV (15 h of counting). The 336.2-keV line corresponds to the deexcitation of the ^{115m}In isomer.

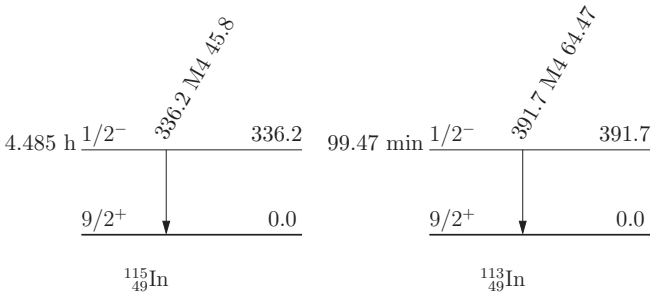

FIG. 3. Partial level schemes of ^{115}In and ^{113}In from Refs. [23] and [24], respectively.

decay to excited states of ^{114}Cd. The corresponding γ rays are at 558.4 and 725.3 keV [25].

The ^{113}In(γ,n) reaction produces the unstable ^{112gs}In with a lifetime of about 15 min and the first isomeric state ^{112m}In, at 156.6 keV, with a lifetime of about 20 min (see Fig. 5). The ^{112gs}In decays to ^{112}Cd by electron capture or β^+ decay, which induces γ rays at 606.8 and 617.1 keV [26].

Additional γ rays at 355.4, 416.8, 463.2, 818.7, 1097.3, 1293.5, and 1507.6 keV are observed in the decay spectrum of Fig. 2. They correspond to transitions of ^{116}In [27], which is produced by ^{115}In(n,γ) reactions. The 511-keV emission coming from positron annihilation is also visible.

B. Activation yields

The photoactivation yield of a radionuclide, $Y_{\rm act}$, produced at the electron energy E_e is proportional to the integrated product between the Bremsstrahlung distribution of the impinging photons, dN_γ/dE_γ, and the activation cross section $\sigma(E_\gamma)$, over the photon energy range, from the reaction threshold

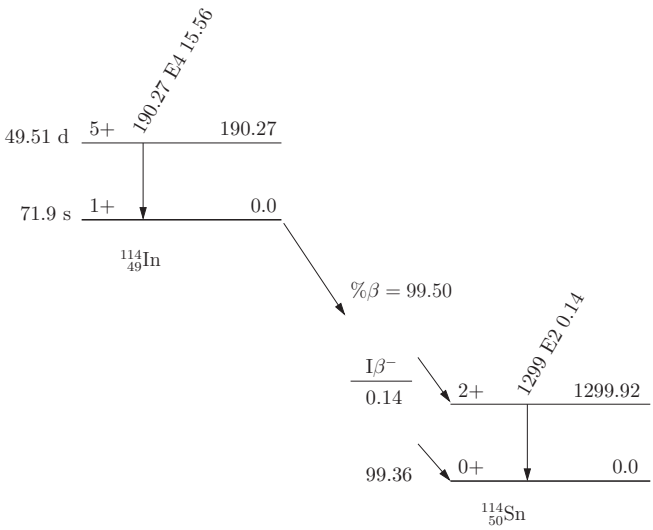

FIG. 4. Partial level scheme of ^{114}In with the β^- decay onto ^{114}Sn from Ref. [25].

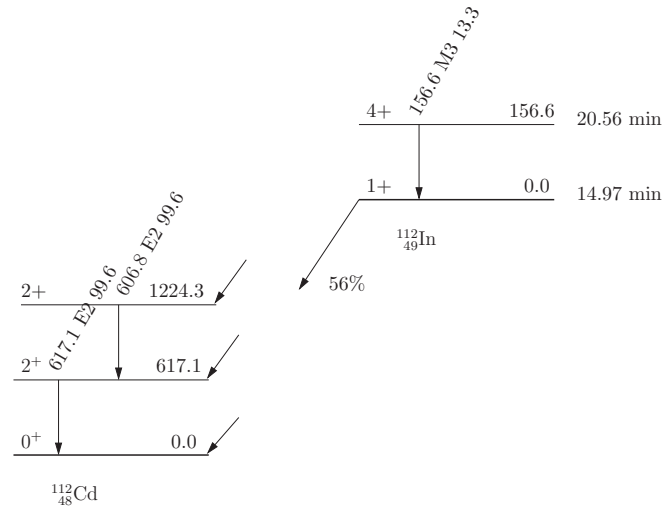

FIG. 5. Partial level scheme of ^{112}In with the β^+ decay onto ^{112}Cd from Ref. [26].

energy $E_{\rm thres}$ to the endpoint energy E_e:

$$Y_{\rm act}(E_e) = N_{tgt} \int_{E_{\rm thres}}^{E_e} \frac{dN_\gamma}{dE_\gamma}(E_\gamma, E_e)\sigma(E_\gamma) dE_\gamma, \qquad (1)$$

where E_γ is the photon energy and $N_{\rm tgt}$ is the target areal density. This yield can be expressed per μC of incident electron beam when the Bremsstrahlung spectrum is normalized to the total electron beam charge. Usually, the activation cross section $\sigma(E_\gamma)$ is extracted as a function of E_γ by unfolding the integral. This unfolding requires both precise knowledge of the photon beam spectrum, especially close to the endpoint energy, and yield data with high counting statistics on a fine grid of endpoint energies [27–29]. In this work, this approach was not adopted, and the measured yields of photoexcited ^{115m}In are rather compared to expected yields calculated following Eq. (1) using different cross sections, which depend on the PSF model.

The measured yields $Y_{\rm act}$ are obtained from the measured number of counts in the full-energy peak corresponding to the radionuclide decay N_γ by

$$Y_{\rm act}(E_e) = \frac{t_{\rm irr}}{Q} \frac{\lambda}{1 - e^{-\lambda t_{\rm irr}}} e^{\lambda t_{\rm loss}} \frac{N_\gamma(E_e) - N_{bg}}{I_\gamma \epsilon (1 - e^{-\lambda t_{\rm meas}})} \qquad (2)$$

if the radionuclide is populated by only one process. In Eq. (2), $t_{\rm meas}$ is the duration of counting, I_γ is the absolute γ-ray intensity, λ is the decay constant, ϵ is the detector photopeak efficiency, and Q is the total beam charge delivered during irradiation. The background underlying the full-energy peak, $N_{\rm bg}$, is taken into account, as well as decay losses during irradiation ($t_{\rm irr}$) and between the end of irradiation and the beginning of counting ($t_{\rm loss}$). The resulting yields are determined for each target sample and normalized per μC of incident electron beam.

The absolute photopeak efficiencies ϵ of the counting setups are obtained from Monte Carlo simulations to take the extended source geometry into account. The exact dimensions of both HPGe detectors were determined using x-ray

TABLE I. Transitions and corresponding parameters necessary for the determination of activation yields pertinent to this work. See text for details.

Reaction or excitation process	E_γ (keV)	I_γ (%)	ϵ (%)
^{113}In$(\gamma,n)^{112m}$In	156.61 (3)	13.3 (15)	1.82 (3)
^{115}In$(\gamma,n)^{114m}$In	190.27 (3)	15.56 (15)	1.87 (2)
^{115}In$(\gamma,\gamma')^{115m}$In	336.244 (17)	45.8 (22)	1.55 (2)
^{197}Au$(\gamma,n)^{196}$Au	355.73 (5)	87 (3)	0.70 (1)

radiographies to ascertain crystal dimensions, endcap-to-crystal distances, and endcap thicknesses. Simulated efficiencies for pointlike source geometry were calculated with GEANT4, v.9.6.p03 [30]. They were compared to measured data from calibration ^{152}Eu sources to validate the simulation. The energy E_γ and the absolute intensity I_γ of the transitions from the unstable or excited nuclei that pertain to this work are summarized in Table I, with the corresponding efficiencies in the extended source geometry. Uncertainties on the transitions' energies and intensities are adopted from Ref. [23] for ^{115}In, Ref. [31] for ^{112m}In, and Ref. [32] for ^{196}Au. The efficiencies depend on E_γ and on the HPGe detector. They are 1.55(2)% for the 336-keV γ ray of In and 0.70(1)% for the 356-keV γ ray of Au. The associated uncertainties are related to statistics and to a systematic correction factor determined from the pointlike source calibration of the simulation.

C. The Bremsstrahlung spectra

The photon spectra were simulated at the irradiation site using GEANT4. Monoenergetic electrons were propagated into the Bremsstrahlung source geometry, which includes the radiator target, the beam hardener, and all collimators.

The calculated photon spectra impinging on the In sample are presented in Fig. 6 for each electron beam energy and per μC of incident beam charge. These spectra are validated by

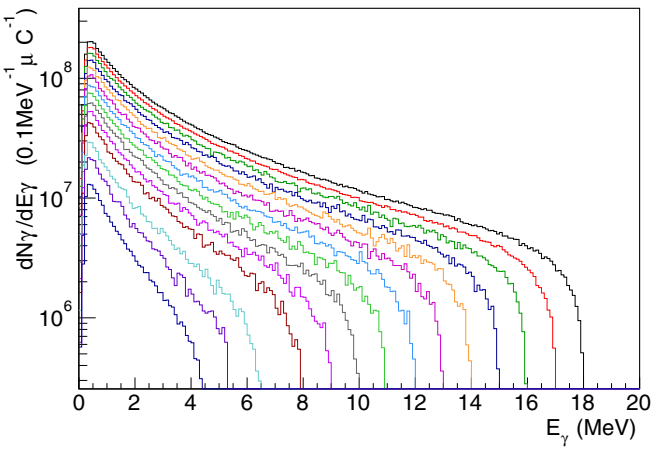

FIG. 6. Bremsstrahlung spectra impinging onto the In sample at the irradiation site obtained from Monte Carlo simulations (GEANT4) for incident electron energies between 4.5 and 18 MeV.

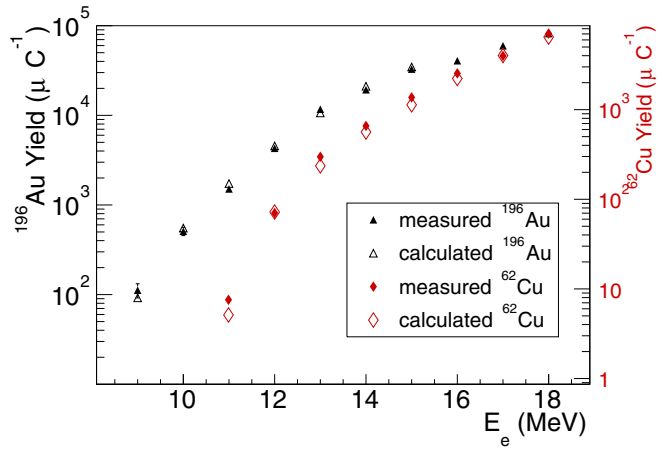

FIG. 7. Measured and calculated yields of activated ^{196}Au and ^{62}Cu as a function of electron beam energies.

comparing the measured and calculated yields of the ^{196}Au and ^{62}Cu activation standards.

The measured and calculated yields are shown in Fig. 7 for both the ^{196}Au and ^{62}Cu nuclei. The measured yields of ^{196}Au are determined from the full-energy peak counts of the 355-keV transition using Eq. (2). The measured yields of ^{62}Cu are determined from the β^+ activity measurements of the Cu targets.

Following the recommendation from Ref. [27], the ^{196}Au calculated yields were obtained using the total measured cross section from Ref. [33], to which a subtraction of 8% was applied. The statistical uncertainty on the calculated Bremsstrahlung spectra and the uncertainty on the reaction cross section are propagated to the calculated yields of ^{196}Au and ^{62}Cu using a full Monte Carlo approach. A random value of the number of photons between energies E_γ and $E_\gamma + dE_\gamma$ is obtained by considering a Gaussian distribution of the number of photons centered on $dN_\gamma(E_\gamma)$ with a standard deviation equal to $\sqrt{dN_\gamma}$. Expected yields of ^{196}Au are only calculated for electron beam energies below 15 MeV, above which a contribution of the $(\gamma,2n)$ reaction affects them, as the reaction threshold equals 14.8 MeV. Calculated and measured ^{196}Au yields agree within uncertainties.

The (γ,n) reaction cross section from Ref. [34] was used for the calculation of expected yields of ^{62}Cu, with an added systematic uncertainty of 8% to render the dispersion between Refs. [35] and [36]. Uncertainties on the expected yields are thus larger than those for the ^{196}Au data. The comparison between calculated and measured yields also agrees within uncertainties, thus validating the calculations of the Bremsstrahlung spectra above the neutron emission threshold energy. We assume that they are also correct at lower energies. A similar approach was adopted in Ref. [37].

D. Neutron production yields

The presence of (n,γ) reaction products in the measured spectra of In (see Fig. 2) shows that low-energy neutrons are present. If neutrons with sufficient energies are also produced, a contribution of ^{115m}In produced by (n,n') inelastic neutron

scattering is expected in the total measured yield of ^{115m}In. Such neutrons are generated by (γ,n) reactions in all materials surrounding the target and within the targets themselves.

To test the production of photoneutrons in the collimators and different beam structures, irradiation configurations were modified. At each electron beam energy, irradiations were performed with and without shielding the targets with a 5-cm-thick block of polyethylene, acting as a neutron moderator, and a 1-cm-thick foil of cadmium, acting as an absorber of the moderated neutrons. This shielding was placed in the beam path in front of the In sample. Monte Carlo simulations of the Bremsstrahlung spectrum at the irradiation site with and without the shielding were calculated using GEANT4. These simulations showed that the expected impact of the shielding on the photon spectrum is a constant transmission of $90 \pm 7\%$ over all photon energies. The uncertainty corresponds to the standard deviation. Similar simulations were performed for the expected neutron spectrum using MCNPX. The ratio between calculated neutron spectra with and without the shielding is $30 \pm 10\%$ over all neutron energies. The uncertainty also corresponds to the standard deviation over the continuous spectrum of neutrons. These ratios are compared to the mean ratio of total measured yields of ^{115m}In with and without the shielding over all electron beam energies. This ratio is $89 \pm 1\%$, the uncertainty of which corresponds to standard deviation. The loss in ^{115m}In yield with the shielding is thus compatible with the calculated loss in the γ beam. The (n,n') cross section is of the order of 300 mb over the 2 to 10 MeV neutron energy range [38], which is about 2 orders of magnitude larger than the maximum value of the published (γ,γ') cross sections, which is of the order of a few millibarns [14,15,19,20]. The attenuation of the measured yields is thus not compatible with the expected attenuation of an impinging neutron spectrum, and the contribution of (n,n') excitations induced by neutrons coming from the beam structures is neglected in the following.

Photoneutrons produced in the Au and Cu targets irradiated alongside the In target are determined from the measurements of the ^{197}Au$(\gamma,n)^{196}$Au, ^{65}Cu$(\gamma,n)^{64}$Cu, and ^{63}Cu$(\gamma,n)^{62}$Cu activation yields, as already described in Sec. III C.

Within the In target itself, photoneutrons are expected from the ^{113}In$(\gamma,n)^{112m}$In, ^{113}In$(\gamma,n)^{112gs}$In, ^{115}In$(\gamma,n)^{114m}$In, and ^{115}In$(\gamma,n)^{114gs}$In reactions.

The production yield of ^{112m}In is determined from the 156-keV γ-ray counting, while the yield for ^{112gs}In is obtained from a fit of the time decay of the ^{112}Cd 617-keV γ ray. Figure 8 shows an example of such a fit, with residuals plotted at the bottom of the figure. Both yields of ^{112m}In and ^{112gs}In are considered as parameters for the fit, and residuals exhibit a fully statistical behavior. The production yields of ^{112m}In extracted from the fit are compared to the ones obtained from the analysis of the 156-keV γ ray. Both methods give compatible production yields of the ^{112m}In isomer within uncertainties and so validate the yields of ^{112gs}In.

The measured yields of ^{114m}In are obtained from the 190-keV γ-ray counting, but the yields of ^{114gs}In could not directly be extracted from measured data, because the ^{114gs}In mainly decays to the stable ^{114gs}Sn with a half-life of about 71 ns (see Fig. 4). An expected ratio between ^{114gs}In and

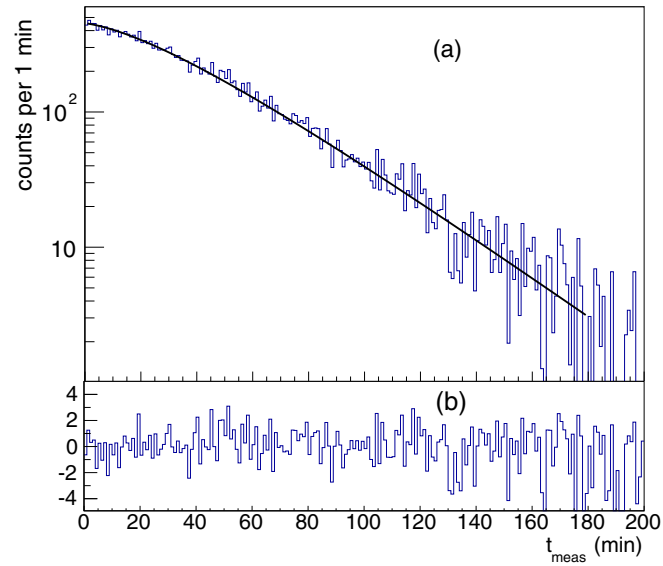

FIG. 8. (a) Time decay spectrum of the 617-keV γ ray of ^{112}Cd fitted by the expected analytical expression of the decay taking the ^{112m}In and ^{112gs}In production yields as parameters. (b) Residuals of the fit.

^{114m}In production yields is thus calculated using Eq. (1). The photon fluxes presented in Sec. III C. and cross sections of the ^{115}In$(\gamma,n)^{114gs}$In and ^{115}In$(\gamma,n)^{114m}$In reactions calculated using the TALYS code are used. Input parameters of TALYS are discussed in Sec. IV. The calculated ratio between ^{114gs}In and ^{114m}In yields is of the order of 27% over the 10 to 18 MeV energy range. This ratio is applied to the measured yields of ^{114m}In to obtain the yields for ^{114gs}In.

Figure 9 shows all obtained (γ,n) yields on a logarithmic scale. Uncertainties are a combination of statistics and systematics due to detection efficiencies. They amount to about 10% of the data for ^{114m}In and are smaller than the data

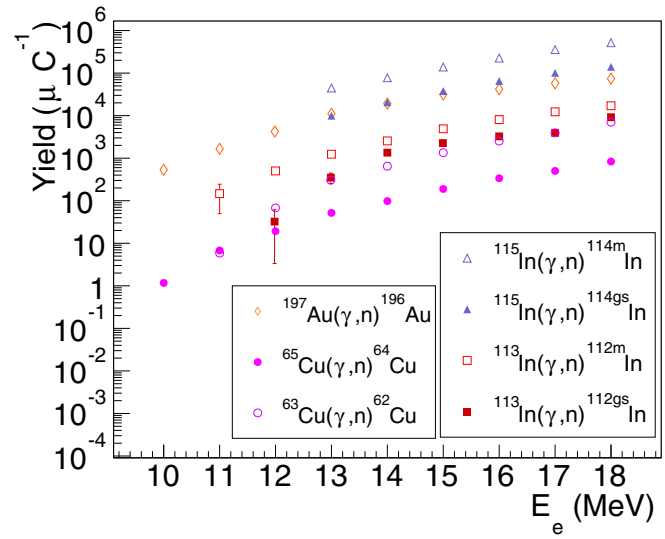

FIG. 9. Yields of (γ,n) reactions in the In, Au, and Cu targets per μC of electron beam.

points on the logarithmic scale. The ^{114m}In production yield reaches 5×10^5 μC^{-1} at 18 MeV and is five to seven times greater than the ^{196}Au yield. Uncertainties on the ^{196}Au yield amount to 8% of the data. The measured production yields of ^{112m}In are about 20% of the ^{196}Au yields, whereas the ^{112gs}In and ^{62}Cu yields are about 1 to 2 orders of magnitude lower. Uncertainties are 6 to 10% of the data for ^{112m}In and ^{112gs}In and 4% for ^{62}Cu. Adding all photoneutron sources, the total neutron yield produced in the In, Au, and Cu targets at 18 MeV is a little above 7×10^5 neutrons per μC of electron beam. The corresponding photon yield is 5×10^9 photons per μC in the 18-MeV Bremsstrahlung spectrum. As mentioned above, the (n,n') cross section is of the order of 0.3 b in the 2 to 10 MeV energy range [38,39] and is about 2 orders of magnitude greater than the published photoexcitation cross sections [14,15]. The neutron yield can thus not be neglected in the production of ^{115m}In.

E. ^{115m}In measured yields

The TALYS code, GEANT4 Monte Carlo simulations, and the (γ,n) yields presented in the previous section are used to estimate the ^{115}In$(n,n')^{115m}$In contribution to the total measured ^{115m}In yield.

TALYS is used to determine the energy distributions of photoneutrons emitted by (γ,n) reactions on In and Au nuclei. The code calculates the differential cross sections of the reactions at a given photon energy E_γ: $d\sigma(E_\gamma,E_n)/dE_n$, where E_n is the emitted neutron energy. The input parameters of the code are described in Sec. IV. When considering continuous Bremsstrahlung photon energy spectra, the energy distribution of the emitted photoneutrons is given by

$$\frac{dN_n}{dE_n}(E_e,E_n) = N_{\rm tgt}\int_0^{E_e}\frac{dN_\gamma(E_\gamma)}{dE_\gamma}\,\frac{d\sigma(E_\gamma,E_n)}{dE_n}\,dE_\gamma, \quad (3)$$

where $N_{\rm tgt}$ is the target areal density and E_e is the electron beam energy. Figure 10(a) shows the resulting energy distributions of photoneutrons produced in the In target by the $^{\rm nat}$In(γ,n) reactions. These distributions present a maximum at low energy, between 0.2 and 0.6 MeV depending on the electron beam energy. Similar distributions are calculated for photoneutrons produced in the Au target.

Monte Carlo simulations are necessary to propagate photoneutrons emitted in each target and evaluate the yield of ^{115}In$(n,n')^{115m}$In excitations. GEANT4 contains the total inelastic scattering cross section on natural In and thus cannot be used to directly obtain the yield of ^{115}In$(n,n')^{115m}$In. It is used to determine the energy distributions of the photoneutrons that interact by inelastic scattering in the In sample. The total inelastic cross section implemented in GEANT4 is checked and shown to be of the same order of magnitude as measured values [40,41] and values calculated with TALYS in the 4 to 18 MeV energy range of interest in this work. Neutrons are emitted isotropically and homogeneously within each target volume and propagated with incident energies following the distributions determined using Eq. (3). The energy distributions of neutrons emitted in the In sample and interacting by inelastic scattering within the sample are shown in Fig. 10(b). When compared to the incident photoneutron distributions of Fig. 10(a), one can see that only photoneutrons with energies beyond 1 MeV undergo inelastic processes.

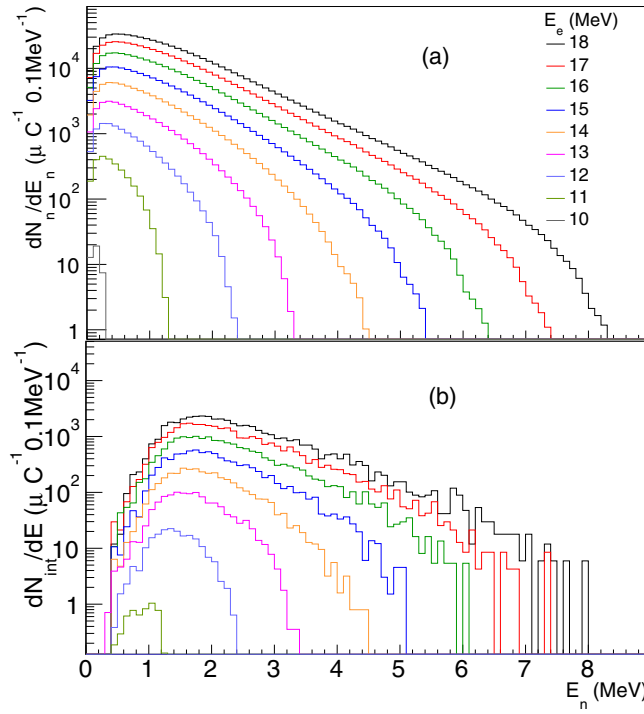

FIG. 10. Energy distributions of (a) photoneutrons produced by all (γ,n) reactions in the natural In sample. (b) Photoneutrons produced in the In sample and interacting by inelastic scattering in the sample ($dN_{\rm int}/dE$).

Finally, to obtain the ^{115}In$(n,n')^{115m}$In excitation yield, a probability of interaction by the (n,n') inelastic scattering process leading to ^{115m}In is determined per incident photoneutron. This probability, $p_{nn'}$, is calculated using the energy distributions of interacting neutrons, $dN_{\rm int}/dE_n$, the total inelastic cross section on natural In $\sigma^{\rm nat}_{\rm inel}$ used in GEANT4, and the (n,n') inelastic scattering cross section on ^{115}In from Ref. [38], $\sigma^{115m}_{nn'}$:

$$p_{nn'} = \frac{1}{N_n}\int_0^{E_{\rm max}}\frac{dN_{\rm int}}{dE_n}\,\frac{R_{115}\,\sigma^{115m}_{nn'}(E_n)}{\sigma^{\rm nat}_{\rm inel}(E_n)}\,dE_n, \quad (4)$$

where N_n is the arbitrary number of neutrons propagated in the GEANT4 simulation and R_{115} is the isotopic ratio of ^{115}In in natural In. The $\sigma^{115m}_{nn'}$ cross section is interpolated from Ref. [38] because it is in good agreement with all evaluated data available in the ENDF database [39]. The resulting probability of production of ^{115m}In in the In target per incident photoneutron is shown in Fig. 11 as a function of electron beam energy and for photoneutrons produced in either the In or the Au targets. Statistical uncertainties on the energy distributions of the interacting neutrons and uncertainties on the cross sections are propagated quadratically and are smaller than the data points. The probability increases with beam energy and reaches 0.16% at maximum, when the photoneutron is produced in the In target by photons of the 18-MeV Bremsstrahlung spectrum.

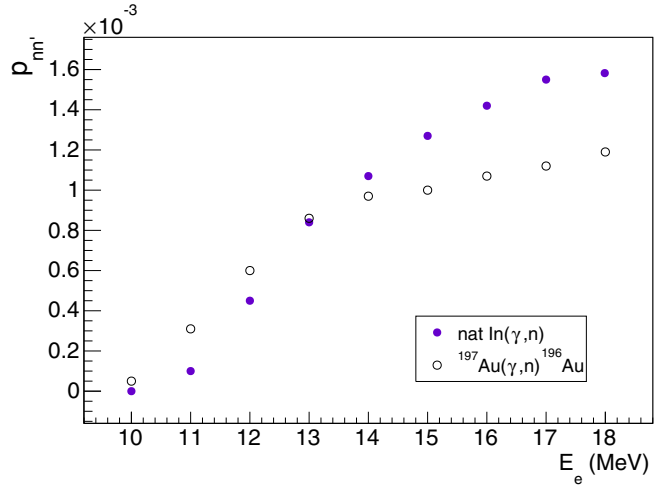

FIG. 11. ^{115}In$(n,n')^{115m}$In excitation probability per photoneutron produced in the In or Au samples. Uncertainties are smaller than the data points.

The probabilities presented in Fig. 11 are applied to the measured neutron production yields presented in Fig. 9 to obtain the (n,n') contribution to the total measured yield of ^{115m}In. Figure 12 presents the measured total and (γ,γ') yields. At 18 MeV, the contribution due to photoneutrons produced by In(γ,n) reactions amounts to 1087 ± 136 μC^{-1}, which corresponds to about 9% of the total measured yield of ^{115m}In, while the contribution from photoneutrons produced in the Au target is of the order of 90 μC^{-1}, which only amounts to about 0.7% of the total measured yield. Considering that the yields of $^{\text{nat}}$Cu(γ,n) reactions are 1 to 2 orders of magnitude lower than the ^{197}Au(γ,n) yields, they are neglected in the correction procedure. Uncertainties on the corrected ^{115}In$(\gamma,\gamma')^{115m}$In yields result from the quadratic propagation of the uncertainties on the photoneutron elastic interaction probability, on the (γ,n) yields, and on the total ^{115m}In yields. They are of the order of 5% of the data.

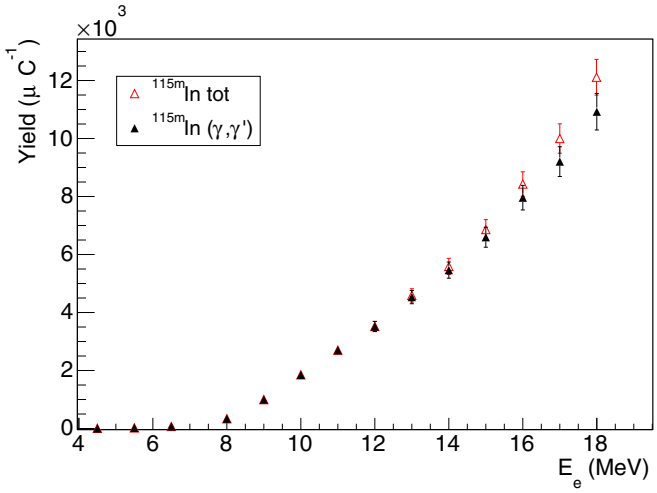

FIG. 12. Measured (γ,γ') yields of ^{115m}In produced in the sample per μC of beam.

IV. RESULTS AND DISCUSSION

A. Comparison with calculations

In this section, the measured photoactivation yields of ^{115m}In are compared to calculated yields. These yields are obtained using (γ,γ') cross sections calculated using TALYS 1.4 [42].

The TALYS code has already been mentioned in this paper, in Secs. III D and III E. Unless otherwise stated, all calculations are performed with the global dispersive optical potential of Morillon and Romain [43], the phenomenological constant temperature model of Gilbert and Cameron [44] for level densities, and the default generalized Lorentzian form of Kopecky and Uhl [45] for the $E1$ PSF. Standard options based on the RIPL database [46] are used for nuclear structure parameters. These input parameters were tested by comparing the calculated cross sections of the total $n + ^{115}$In, the ^{115}In$(n,n')^{115m}$In, and the (γ,n) reactions against available experimental data in the EXFOR database [39]. The calculated ^{115}In$(n,n')^{115m}$In cross section is underestimated by about 20%, indicating a possible problem on the optical potential or level density model. However, variations of the optical potential have a negligible impact on the (γ,γ') cross section of interest in this work. The major contribution to the (γ,γ') yields indeed comes from photons below the neutron separation energy $S_n \simeq 9.5$ MeV. The dependence of the (γ,γ') cross section on available optical potential models was found negligible. The possible influence on level density models is discussed in Sec. IV D.

One of the key ingredients for the calculation of the (γ,γ') cross section is the PSF. Five models are available in TALYS for $E1$ transitions: the standard Lorentzian form (SLO) of the Brink-Axel hypothesis [47,48]; the generalized Lorentzian form (GLO) of Kopecky and Uhl [45]; the spherical Skyrme QRPA calculations, based on Hartree-Fock Bardeen-Cooper-Schrieffer (BCS) solutions or Hartree-Fock Bogolyubov (HFB) solutions [46]; and the Goriely hybrid model [1].

All these models are constrained by (γ,n) data, as the first two ones are fully parametrized to reproduce the data, and the three last ones are tables obtained from microscopic calculations shifted to reproduce the GDR parameters. All radiations other than $E1$, such as $M1$, $E2$, etc., are treated under the Brink-Axel hypothesis and taken into account by the SLO model with parameters from the RIPL systematics. The cross sections of the ^{115}In$(\gamma,n)^{114m}$In reaction are calculated with the five PSF models. The corresponding calculated ^{114m}In yields are compared to the data reported in Fig. 9. They are found in agreement within uncertainties, for all five strength models, as expected from the parametrization of the strengths.

On the contrary, the ^{115}In$(\gamma,\gamma')^{115m}$In cross sections show large discrepancies, up to 1 order of magnitude, depending on the choice of the PSF model, as illustrated in Fig. 13. The calculated cross sections are presented on a logarithmic scale and give qualitatively similar results, exhibiting a maximum at about 9.5 MeV and a local minimum at about 11 MeV. The fall of the cross section at about 9.5 MeV corresponds to the opening of the neutron emission channel, which very quickly overwhelms the γ emission probability. The SLO cross section

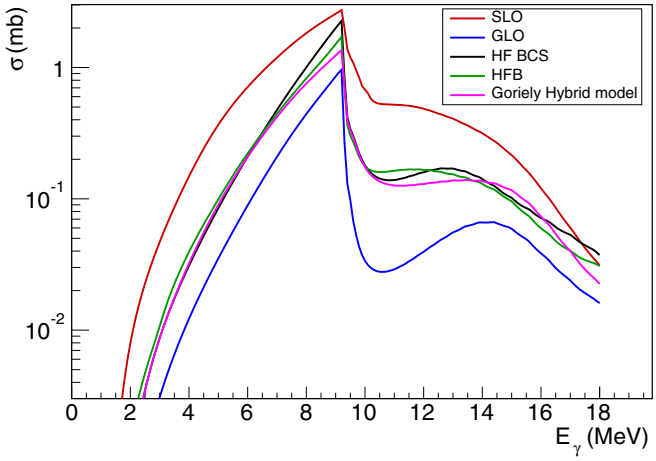

FIG. 13. Cross sections of the ^{115}In$(\gamma,\gamma')^{115m}$In reaction calculated with the TALYS code using the different available models of the PSF. See text for details.

reaches 2.7 mb at maximum and is a factor of 3 larger than the maximum value of the GLO result. More than 1 order of magnitude separates the local minima of these two cross sections around 11 MeV. All the other results lie in between these extrema and are similar to one another.

The calculated and measured photoexcitation yields of ^{115m}In are presented in Fig. 14 as a function of electron beam energy. The plot inset presents the lower energy points on a logarithmic scale. Statistical uncertainties on the Bremsstrahlung spectra are propagated as detailed in Sec. III C, but are negligible. Although the increase of the data with beam energy is reproduced, none of the calculated yields quantitatively reproduce the data on the whole energy range. The SLO overestimates the cross section and thus the yields, while the GLO calculation underestimates the yields by at least a factor of 4. All other PSF models agree with the data below 6.5 MeV and underestimate the yields at higher energies by about a factor of 2.

B. Low-energy enhancement in the photon strength

Results on ^{112}Cd [7] and ^{116}Sn [8,9] suggest that additional strength could be expected for ^{115}In at energies between 6 and 10 MeV. In these studies, nuclear level densities and PSFs below the neutron separation energy are extracted from $(^3\mathrm{He},\alpha\gamma)$ and $(^3\mathrm{He},{}^3\mathrm{He}'\gamma)$ reaction data using the Oslo method [11]. Additional dipole strength is introduced on top of the GLO $E1$ PSF to reproduce the data, in the form of a Gaussian contribution. A best fit to the ^{112}Cd data is obtained with the Gaussian contribution centered at 8.7(2) MeV, with a standard deviation of 1.5(1) MeV and an integral of $3.7(3)\times10^{-7}$ MeV^{-2}. The additional strength necessary to reproduce the ^{116}Sn is comparable, with a standard deviation of 1.4(1) MeV and an integral of $3.2^{+3}_{-9}\times10^{-7}$ MeV^{-2} [9], but is centered a little lower in energy at 8.0(1) MeV.

A similar approach is adopted to reproduce our data. A Lorentz function is introduced in the PSF. It is added either to the $E1$ GLO model or to the default $M1$ SLO model in TALYS, to test the possible dependence on electromagnetic nature. The parameters of this Lorentzian are adjusted to fit the photoexcited ^{115m}In yields. A χ^2 between calculated and measured yields is minimized to determine the Lorentz function parameters. In the following, the added resonance is referred to as a "PDR" or a "pygmy" when it is introduced in the $E1$ PSF and as a "Lorentzian" when it is introduced in the $M1$ PSF.

Figure 15 shows the measured and calculated yields for which the minimum χ^2 value is obtained, with the lower energy points on a logarithmic scale in the inset. The calculated yields obtained using the GLO $E1$ PSF and a PDR are practically undistinguishable from the yields obtained using the GLO $E1$ PSF and an additional Lorentzian in the $M1$

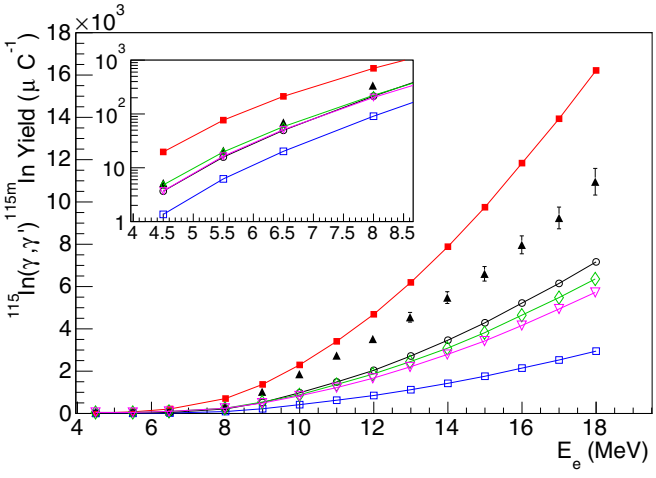

FIG. 14. Comparison between the measured photoexcitation yields of ^{115m}In (solid black triangles) and simulated yields, calculated with the different PSF models available in the standard input parameters of TALYS. Color codes for calculated yields are identical to those in Fig. 13.

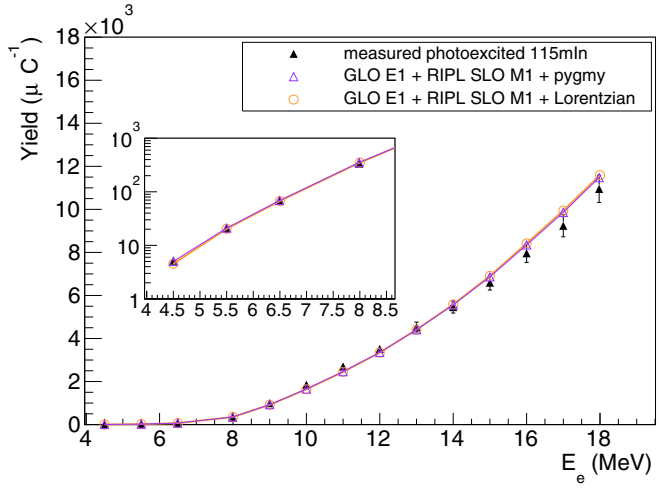

FIG. 15. Comparison between the measured photoexcitation yields of ^{115m}In and calculated yields obtained with the GLO $E1$ and the default SLO $M1$ PSFs and with either $E1$ (pygmy) or $M1$ additional photon strength. See text for details.

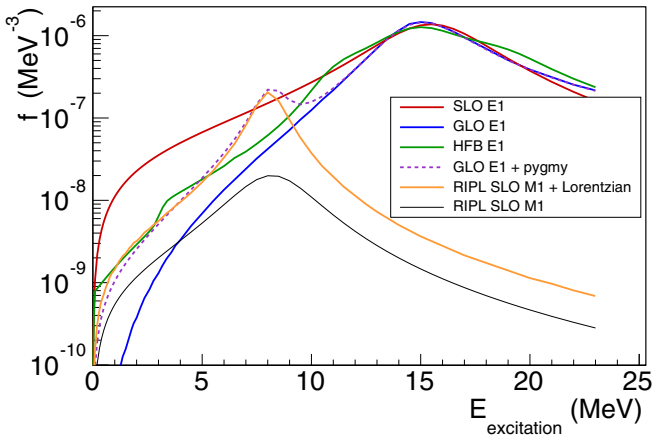

FIG. 16. Photon strength functions used in this work to reproduce the data. See text for details.

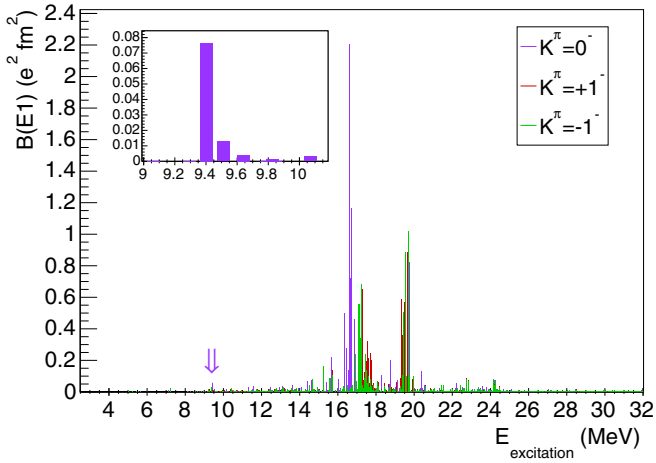

FIG. 17. $B(E1)$ reduced transition probability in ^{115}In calculated in the QRPA approach with the Gogny D1S force.

strength. The corresponding χ^2/ndf values are 0.9 and 1.2, respectively. The calculated yields are slightly overestimated above 16 MeV but remain within experimental uncertainties and are otherwise in very good agreement with the data over the whole energy range. Either $E1$ or $M1$ electromagnetic natures for the additional strength allow the data to be reproduced.

The corresponding PSFs are shown in Fig. 16. The PSFs from the SLO and HFB models for the $E1$ strength are also plotted for comparison. The additional strength is centered at 8.2 MeV, with a width of 1.7 MeV, when it is introduced on top of the GLO $E1$ PSF. It is centered at 8.1 MeV, with a width of 1.6 MeV, when it is introduced on top of the SLO $M1$ PSF. In both cases, the additional strength reaches 1.8×10^{-7} MeV^{-3} at maximum. This is 1 order of magnitude larger than the 2.0×10^{-8} MeV^{-3} maximum value of the default SLO $M1$ strength from the RIPL database [46].

The additional strength is positioned at energies comparable to the PDR observed in ^{116}Sn at 8.0(1) MeV [8,9], while the PDR observed in ^{112}Cd is positioned at 8.7(2) MeV [7]. The total additional strength is 4.6×10^{-7} MeV^{-2} when added to the $E1$ GLO PSF or 4.3×10^{-7} MeV^{-2} when added to the $M1$ SLO PSF. It is of the same order of magnitude as the PDRs observed in ^{116}Sn ($3.2^{+3}_{-9} \times 10^{-7}$ MeV^{-2}) and ^{112}Cd ($3.7(3) \times 10^{-7}$ MeV^{-2}) [7]. Because either the $E1$ or the $M1$ transition character allows the ^{115m}In data to be reproduced, the electromagnetic nature of the additional strength is still indefinite. Complementary data that would allow the determination of the $E1$ or the $M1$ character are necessary for clarification, as in the case of Sn, for which the $E1$ character of the PDRs was identified using NRF data [10].

C. Microscopic calculations

New fully microscopic reduced transition probabilites are calculated for the ^{115}In odd-even nucleus to see if compatible additional strength is predicted in the 7 to 9 MeV PDR energy range or in the corresponding $M1$ energy range. The PSF $f^{(\Pi L)}$ ($\Pi = E$ or M) is obtained by averaging these reduced transition probabilities over an excitation energy interval Δ [49]:

$$\frac{1}{\Delta}\sum_{\Delta} B(E1)\downarrow (e^2\,\mathrm{fm}^2) = 0.955 \times 10^6\ f^{(E1)}\,(\mathrm{MeV})^{-3},$$

$$\frac{1}{\Delta}\sum_{\Delta} B(M1)\downarrow \left(\mu_N^2\right) = 86.6 \times 10^6\ f^{(M1)}\,(\mathrm{MeV})^{-3},$$

with $B(\Pi L)\uparrow = \frac{2J+1}{2J_0+1} B(\Pi L)\downarrow$, considering J_0 as the ground-state total angular momentum and J that of the excited state.

A fully consistent QRPA calculation based on HFB states is performed [50], using the finite-range Gogny D1S effective force [51–53]. This approach allows the treatment of Hartree-Fock mean field and pairing correlations on the same footing and the inclusion of all residual parts of the interaction without any truncation in QRPA matrices. For a detailed description of the corresponding formalism for even-even nuclei, see Ref. [54]. In the particular case of ^{115}In, which is an odd-even nucleus, the blocking technique is used on HFB calculations. The extra proton is singled out of the QRPA valence space as suggested in Ref. [55] for charge exchange calculations. This general blocking technique induces a time-reversal symmetry breaking. As a consequence, the usual degeneracy between the different projections K of the angular momentum on the symmetry axis of the axially symmetric-deformed nucleus is split into $K = 0$ and $K = \pm 1$ values, even for a spherical calculation.

Figure 17 shows the resulting reduced transition probability $B(E1)$ as a function of excitation energy, for $K = 0, \pm 1$. The transitions corresponding to the nuclear GDR lie in the 16 to 20 MeV excitation energy range and are split into two components. The position of the resonance is shifted towards higher energies compared to the experimental value of about 15.5 MeV. This overestimation of the GDR is systematically obtained within the present framework [56]. It is taken care of in the strength determination by a global energy shift of the $B(E1)$ distribution. A vertical arrow points to a transition at 9.4 MeV with a $B(E1) = 7.6 \times 10^{-2}\ e^2\,\mathrm{fm}^2$, presented in the

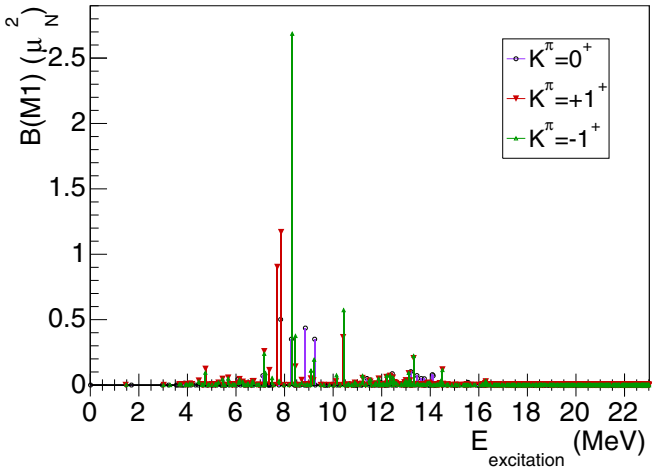

FIG. 18. $B(M1)$ reduced transition probability in ^{115}In calculated within the QRPA approach using the Gogny D1S force.

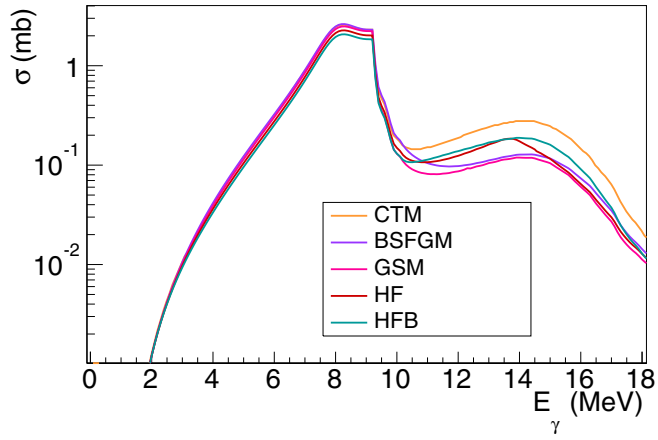

FIG. 19. Cross sections of the ^{115}In$(\gamma,\gamma')^{115m}$In reaction calculated using the different level density models available in the TALYS code. See text for details.

inset, the position in energy of which is compatible with the additional strength observed in the data.

Figure 18 shows first explorative results of the $B(M1)$ spin-flip transition probability distribution obtained within the same QRPA approach, for the $K = 0, \pm 1$ projections. Several transitions between 0.4 and 2.7 μ_N^2 at excitation energies a little below 8 and 10 MeV are predicted. The sum of these transition probabilities is of the same order of magnitude as the $E1$ transition predicted at 9.4 MeV ($1\ \mu_N^2 = 1.105\,710^{-2}\ e^2\,\mathrm{fm}^2$). The microscopic calculations in the QRPA approach predict transitions from both electric dipole and spin-flip origins at energies that are compatible with the necessary additional strength observed in the data and do not allow the identification of the one contribution over the other.

D. Level density models

The calculated yields presented in Fig. 15 agree with the data within uncertainties, but a slight systematic overestimation is observable above $E_e = 16$ MeV. These energies correspond to photon energies close to the $E1$ GDR maximum, where the PSF well describes the (γ,n) data. The deviation might thus indicate a sensitivity to the nuclear level density model. As already mentioned, the (γ,γ') cross sections are calculated using the phenomenological constant temperature model (CTM) of Gilbert and Cameron [44]. This model consists in dividing the nuclear level density into two regions: below an excitation energy E_M the constant temperature law applies, and the Fermi gas model is used above. In our case, the excitation energy E_M is 4.45 MeV. Four other nuclear level density models are available in TALYS [42,57]. The back-shifted Fermi gas model (BSFGM) and the generalized superfluid model (GSM) are phenomenological. Microscopic calculations on the basis of Hartree-Fock solutions (HF) [58] and energy-, spin-, and parity-dependent calculations based on the microscopic combinatorial model are also available (HFB). The latter makes coherent use of nuclear structure properties determined within the deformed Skyrme-Hartree-Fock-Bogolyubov framework [59]. Unless otherwise stated, all following calculations were performed with the GLO model for the $E1$ PSF and the SLO model for the $M1$ PSF enhanced as detailed in Sec. IV B.

Figure 19 shows the (γ,γ') cross sections calculated using the different nuclear level density models. All level density models give similar results for photon energies below the neutron emission threshold, with a difference of about 20% at the most between the BSFGM and the HFB model below 9.5 MeV. Larger discrepancies can be seen above 9.5 MeV, with a more than 50% difference between the CTM and the GSM at about 14 MeV.

The corresponding ^{115m}In expected yields are presented in Fig. 20 along with the data. All nuclear level density models allow the expected yields to reproduce the data within uncertainties, except for the HFB model. Although within

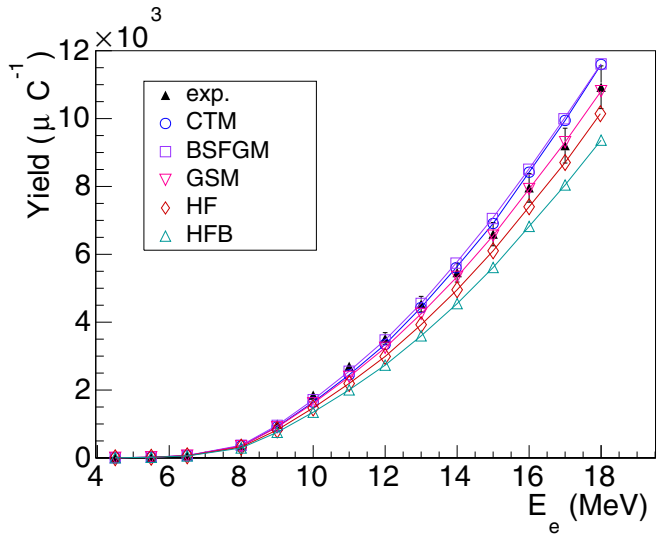

FIG. 20. Comparison between the measured photoexcitation yields of ^{115m}In and calculated yields obtained with the different nuclear level density models available in TALYS and the modified PSF introduced in this work. See text for details.

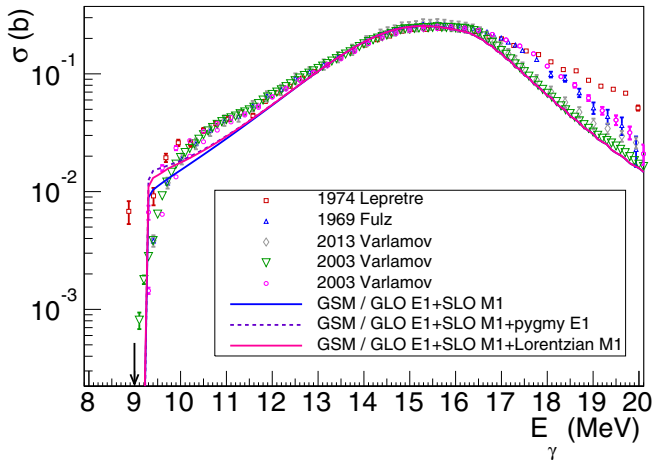

FIG. 21. Total cross section of the ^{115}In(γ,n) reaction calculated using the GLO $E1$ strength function and the default SLO $M1$ strength function, and with either $E1$ (pygmy) or $M1$ additional strength. A vertical arrow points to the neutron separation energy.

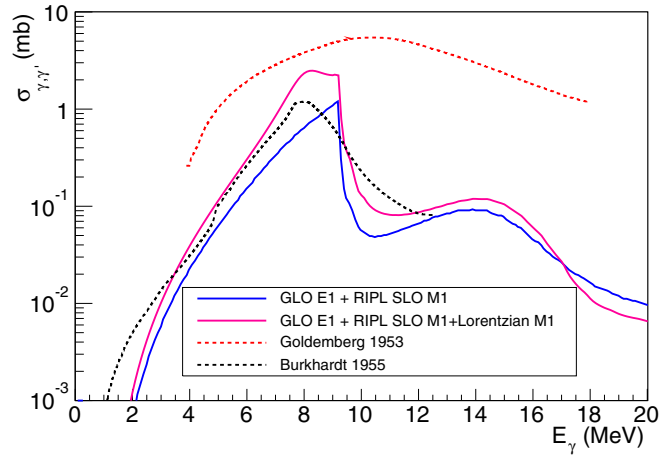

FIG. 22. Experimental and calculated cross sections of ^{115}In$(\gamma,\gamma')^{115m}$In obtained using the GLO model for the $E1$ PSF and either the default SLO $M1$ or the enhanced $M1$ photon strength (Goldemberg and Katz 1953: [14]; Burkhardt *et al.* 1955: [15]).

uncertainties, the BSFGM seems to exhibit a systematic overestimation of the yields above 16 MeV, similar to the one observed with the CTM, and the HF model exhibits a systematic underestimation. The GSM allows however the exact reproduction of the measured yields on the whole energy range. The combination of the GSM for nuclear level densities and the enhanced $M1$ PSF thus allows a perfect reproduction of the photoexcitation data of ^{115m}In.

E. Cross sections

In this section, the total ^{115}In(γ,n) and ^{115}In$(\gamma,\gamma')^{115m}$In cross sections calculated using the modified PSFs are compared to available experimental data. In Fig. 21, the total ^{115}In(γ,n) cross section is calculated with TALYS using three different strength combinations: the GLO model for the $E1$ PSF and the default SLO model for the $M1$ PSF, the GLO with the PDR for the $E1$ strength and the default $M1$ SLO, and finally the GLO for $E1$ and the $M1$ SLO with the additional strength presented in Fig. 16. These calculations are compared to measured data available in the EXFOR database [39]. All three calculations are very similar to one another, because the additional strength introduced at 8.2 MeV impacts very little the PSF above the neutron threshold energy. All of them remain compatible with the experiment within uncertainties in the GDR energy region and with two datasets at higher energies. However, all three fail to reproduce the data around 11 MeV, where there is about a factor of 2 between calculated and measured cross sections.

The ^{115}In$(\gamma,\gamma')^{115m}$In cross section is strongly affected by the additional strength. Figure 22 shows the photoexcitation cross sections calculated using the GLO model for the $E1$ PSF, and either the SLO (blue) or the enhanced SLO $M1$ strength (pink). We remind that the introduction of a PDR in the $E1$ PSF on top of the GLO model is undistinguishable from the latter. The enhancement in the rising of the cross section between 2 and 8 MeV and the shoulder at about 8 MeV due to the additional strength are clearly visible. Experimental data from Refs. [14,15] are also presented. The data from Ref. [15] mostly lie between the two calculated cross sections, except below 3 MeV and between about 10 and 12 MeV. Burkhardt *et al.* estimate the uncertainty in the peak region at ~30% and the uncertainty on the position and full width at half maximum of the peak to be ±1 MeV [15]. Considering these uncertainties, the data from Ref. [15] are compatible with both calculations in the 3 to 9.5 MeV region. The data from Ref. [14] are higher than both calculations, with a maximum value of 5.4 mb positioned at about 10.2 MeV with a width at half maximum of 7.5 MeV. Johns *et al.* mention that the uncertainty associated with their method of extraction of the cross section from the activation data can reach up to 50% [60]. Burkhardt *et al.* [15] discuss the data from Ref. [14] and argue that they are overestimated. The peak value should be at 2.2 mb [15] and the width of the peak should be narrower (see Ref. [15] for details). Taking these corrections into account, the results from Ref. [14] are closer to our calculations with additional strength.

Finally, our results can be compared to the effective integrated cross section $(\sigma\Gamma)$ defined in Ref. [13] by Carroll *et al.* as

$$(\sigma\Gamma) \equiv \sum_j (\sigma\Gamma)_{fj} \frac{F(E_j,E_0)}{F(2.125,E_0)}, \tag{5}$$

where $(\sigma\Gamma)_{fj}$ is the integrated cross section for the excitation of final state f through the jth gateway state. Parts of the population of these gateway states make transitions to the final state either directly or as part of cascade transitions. In Eq. (5), $F(E,E_0)$ is the normalized Bremsstrahlung spectrum of the endpoint energy E_0. The choice of normalizing the intensities of the Bremsstrahlung spectra to 2.125 MeV is arbitrary and was chosen to be less than the gateway energies E_j [13]. Figure 23 shows the comparison between the values of $(\sigma\Gamma)$ in mb keV obtained at $E_0 = 4$ and 6 MeV by Carroll *et al.* and obtained in this work between 4 and 7 MeV, using the photoexcitation cross sections presented in Fig. 22.

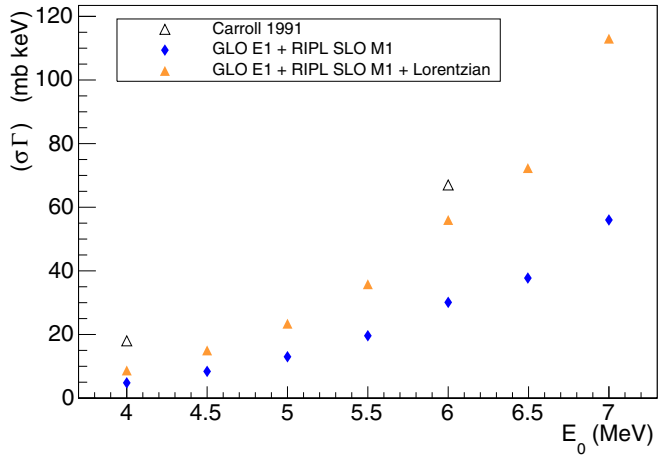

FIG. 23. Effective integrated cross section as a function of the Bremsstrahlung spectrum endpoint energy E_0. See text for details (Carroll *et al.* 1991: [13]).

The values of $(\sigma\Gamma)$ obtained with the photoexcitation cross section calculated with the enhanced strength show a better agreement with the results from Ref. [13]. The values strongly depend on the endpoint energy of the Bremsstrahlung spectrum, and it seems that the results from Ref. [13] at 4 and 6 MeV are closer to ours at 4.5 and 6.5 MeV. The results from Ref. [13] are obtained with the Bremsstrahlung spectra from a Varian Clinac 4/100 linac at 4 MeV and from a Varian Clinac 1800 linac at 6 MeV, but no discussion about the uncertainty on the endpoint energy of the Bremsstrahlung spectra delivered by these linacs allows us to further discuss this observation.

V. CONCLUSION

Production yields of the ^{115m}In isomer by photoexcitation have been measured over an energy range between 4.5 and 18 MeV using a Bremsstrahlung photon source. Special attention was paid to correct the total measured yields from the ^{115}In$(n,n')^{115m}$In contribution. Simulated yields have been calculated using Monte Carlo simulations of the Bremsstrahlung source and calculated cross sections determined using the five PSF models available in the standard input parameters of the TALYS code for the $E1$ strength. None of these simulated yields were able to reproduce the data.

The introduction of additional strength is necessary for the data to be reproduced. This strength can be added either to the $E1$ PSF, on top of the GLO model, or to the $M1$ PSF, on top of the SLO model. It is introduced in the form of a Lorentzian contribution, centered at 8.2 MeV with a width of 1.7 MeV when added to the $E1$ PSF, or centered at 8.1 MeV with a width of 1.6 MeV when added to the $M1$ PSF. The total integrated additional strength is about 4×10^{-7} MeV^{-2} in either case and is compatible with previous results on ^{116}Sn [8,9] and ^{112}Cd [7]. The sensitivity of these results to nuclear level density (NLD) models was investigated. Although the simulated yields weakly depend on the choice of NLD model, the combination of the generalized superfluid model with the additional strength allows the perfect reproduction of the measured yields over the whole energy range.

The agreement between the calculated total (γ,n) cross section and the data is not affected by the modification of the PSF. The region near the GDR maximum is well reproduced, but a difference of about 50% can be observed around 11 MeV. A systematic study of a combined photon strength model that would interpolate between our result for excitation energies between 7 and 9 MeV and the SLO model for excitation energies above 9 MeV should be performed to reproduce the (γ,n) and (γ,γ') data.

QRPA calculations were performed to check for predicted transitions compatible with the observed additional strength and to try to identify the electromagnetic nature of this added strength. Notable $M1$ transitions are predicted between 8 and 10 MeV and one $E1$ transition at 9.404 MeV is compatible with the experiment. Because our data are not sensitive to the multipolarity of the strength, as we have no angular distribution or parity measurements for the measured deexcitation γ rays, and considering that the spin-flip $M1$ giant resonance description within the QRPA approach is still a work in progress [61], additional experimental data are necessary to test the electromagnetic nature of the additional strength introduced to reproduce our data.

Finally, the photoexcitation cross section calculated with the enhanced strength is compared to previous experimental results from Refs. [13–15] and is found to be in agreement within uncertainties, when suggested corrections from Ref. [15] to the data from Ref. [14] are taken into account.

ACKNOWLEDGMENTS

The authors would like to thank A. Binet and J. P. Nègre for providing excellent beam conditions and support. They are also very grateful to B. Rossé for the loan of a HPGe detector, to S. Léoni and D. Filipescu for fruitful discussions, and to B. Morillon and S. Goriely for their help with the calculations. This work was supported by Contracts No. ANR-07-JCJC-0158, and Contracts No. 20071304005 of Région Aquitaine, and No. 20111603003 of Région Aquitaine and CEA/DAM Ile-de-France.

[1] S. Goriely, Phys. Lett. B **436**, 10 (1998).

[2] A. Makinaga, R. Massarczyk, R. Schwengner, M. Beard, F. Dönau, M. Anders, D. Bemmerer, R. Beyer, R. Hannaske, A. R. Junghans *et al.*, Phys. Rev. C **90**, 044301 (2014).

[3] F. Giacoppo, F. L. Bello Garrote, T. K. Eriksen, A. Görgen, M. Guttormsen, T. W. Hagen, A. C. Larsen, B. V. Kheswa, M. Klintefjord, P. E. Koehler *et al.*, EPJ Web Conf. **93**, 01039 (2015).

[4] N. Tsoneva, S. Goriely, H. Lenske, and R. Schwengner, Phys. Rev. C **91**, 044318 (2015).
[5] D. Savran, T. Aumann, and A. Zilges, Prog. Part. Nucl. Phys. **70**, 210 (2013).
[6] H. Utsunomiya, S. Goriely, T. Kondo, T. Kaihori, A. Makinaga, S. Goko, H. Akimune, T. Yamagata, H. Toyokawa, T. Matsumoto *et al.*, Phys. Rev. Lett. **100**, 162502 (2008).
[7] A. C. Larsen, I. E. Ruud, A. Bürger, S. Goriely, M. Guttormsen, A. Görgen, T. W. Hagen, S. Harissopulos, H. T. Nyhus, T. Renstrøm *et al.*, Phys. Rev. C **87**, 014319 (2013).
[8] H. K. Toft, A. C. Larsen, U. Agvaanluvsan, A. Bürger, M. Guttormsen, G. E. Mitchell, H. T. Nyhus, A. Schiller, S. Siem, N. U. H. Syed *et al.*, Phys. Rev. C **81**, 064311 (2010).
[9] H. K. Toft, A. C. Larsen, A. Bürger, M. Guttormsen, A. Görgen, H. T. Nyhus, T. Renstrøm, S. Siem, G. M. Tveten, and A. Voinov, Phys. Rev. C **83**, 044320 (2011).
[10] K. Govaert, F. Bauwens, J. Bryssinck, D. De Frenne, E. Jacobs, W. Mondelaers, L. Govor, and V. Y. Ponomarev, Phys. Rev. C **57**, 2229 (1998).
[11] A. C. Larsen, M. Guttormsen, M. Krtička, E. Běták, A. Bürger, A. Görgen, H. T. Nyhus, J. Rekstad, A. Schiller, S. Siem *et al.*, Phys. Rev. C **83**, 034315 (2011).
[12] U. Kneissl, H. Pitz, and A. Zilges, Prog. Part. Nucl. Phys. **37**, 349 (1996).
[13] J. J. Carroll, M. J. Byrd, D. G. Richmond, T. W. Sinor, K. N. Taylor, W. L. Hodge, Y. Paiss, C. D. Eberhard, J. A. Anderson, C. B. Collins *et al.*, Phys. Rev. C **43**, 1238 (1991).
[14] J. Goldemberg and L. Katz, Phys. Rev. **90**, 308 (1953).
[15] J. Burkhardt, E. J. Winhold, and T. H. Dupree, Phys. Rev. **100**, 199 (1955).
[16] P. von Neumann-Cosel, A. Richter, C. Spieler, W. Ziegler, J. Carroll, T. Sinor, D. Richmond, K. Taylor, C. Collins, and K. Heyde, Phys. Lett. B **266**, 9 (1991).
[17] P. von Neumann-Cosel, V. Y. Ponomarev, A. Richter, and C. Spieler, Z. Phys. A **350**, 303 (1995).
[18] L. Lakosi, J. Sáfár, A. Veres, T. Sekine, H. Kaji, and K. Yoshihara, J. Phys. G: Nucl. Part. Phys. **19**, 1037 (1993).
[19] V. Bokhinyuk, A. Guthy, A. Parlag, M. Sabolchy, I. Sokolyuk, and I. Khimich, Ukr. J. Phys. **51**, 657 (2006).
[20] L. Z. Dzhilavyan, Phys. At. Nucl. **78**, 624 (2015).
[21] A. Chauchat, V. L. Flanchec, A. Binet, J. Flament, P. Balleyguier, J. Brasile, S. Muller, and J. Ortega, Nucl. Instrum. Methods Phys. Res., Sect. A **608**, S99 (2009).
[22] M. Tarisien, C. Plaisir, F. Gobet, F. Hannachi, M. M. Aléonard, and A. Rebii, Rev. Sci. Instrum. **82**, 023302 (2011).
[23] J. Blachot, Nucl. Data Sheets **113**, 2391 (2012).
[24] J. Blachot, Nucl. Data Sheets **111**, 1471 (2010).
[25] J. Blachot, Nucl. Data Sheets **113**, 515 (2012).
[26] D. D. Frenne and E. Jacobs, Nucl. Data Sheets **79**, 639 (1996).
[27] B. L. Berman and S. C. Fultz, Rev. Mod. Phys. **47**, 713 (1975).
[28] C. Nair, M. Erhard, A. R. Junghans, D. Bemmerer, R. Beyer, E. Grosse, J. Klug, K. Kosev, G. Rusev, K. D. Schilling *et al.*, Phys. Rev. C **78**, 055802 (2008).
[29] A. S. Penfold and J. E. Leiss, Phys. Rev. **114**, 1332 (1959).
[30] S. Agostinelli *et al.* (GEANT4 Collaboration), Nucl. Instrum. Methods Phys. Res., Sect. A **506**, 250 (2003).
[31] S. Lalkovski and F. Kondev, Nucl. Data Sheets **124**, 157 (2015).
[32] H. Xiaolong, Nucl. Data Sheets **108**, 1093 (2007).
[33] A. Veyssiere, H. Beil, R. Bergere, P. Carlos, and A. Lepretre, Nucl. Phys. A **159**, 561 (1970).
[34] R. E. Sund, M. P. Baker, L. A. Kull, and R. B. Walton, Phys. Rev. **176**, 1366 (1968).
[35] V. Varlamov, B. Ishkhanov, D. Rudenko, and M. Stepanov, Phys. At. Nucl. **67**, 2107 (2004).
[36] V. V. Varlamov, N. G. Efimkin, B. S. Ishkhanov, V. V. Sapunenko, and M. E. Stepanov, Bull. Russ. Acad. Sci. Phys. **59**, 911 (1995).
[37] C. Plaisir, F. Hannachi, F. Gobet, M. Tarisien, M. Aléonard, V. Méot, G. Gosselin, P. Morel, and B. Morillon, Eur. Phys. J. A **48**, 68 (2012).
[38] A. A. Lapenas, Kh. Ja. Bondars, and J. Vejnbergs, Neutron Spect. Meas. Activ. Riga (1975), data taken from the EXFOR database, file EXFOR V0002.004.
[39] N. Otuka *et al.*, Nucl. Data Sheets **120**, 272 (2014).
[40] G. Lamaze, C. Eisenhauer, J. Grundl, E. McGarry, F. Schima, V. Spiegel, and S. Igarashi, *Cross-Section Measurements in the Intermediate-Energy Standard Neutron Field* (Saikon, Tokyo, 1988).
[41] P. Buchanan, D. Nellis, and W. Tucker, A Compilation of Cross Sections and Angular Distributions of Gamma Rays Produced by Neutron Bombardment of Various Nuclei, Texas Nuclear Corp. Reports, No. 63, (1963), p. 1.
[42] S. H. A. J. Koning and M. Duijvestijn, in *Proceedings of the International Conference on Nuclear Data for Science and Technology April 22–27, 2007, Nice, France*, edited by O. Bersillon, F. Gunsing, E. Bauge, R. Jacqmin, and S. Leray (EDP Sciences, Les Ulis, France, 2008), pp. 211–214.
[43] B. Morillon and P. Romain, Phys. Rev. C **70**, 014601 (2004).
[44] A. Gilbert and A. G. W. Cameron, Can. J. Phys. **43**, 1446 (1965).
[45] J. Kopecky and M. Uhl, Phys. Rev. C **41**, 1941 (1990).
[46] R. Capote *et al.*, Nucl. Data Sheets **110**, 3107 (2009).
[47] D. M. Brink, Ph.D. thesis, Oxford University, 1955.
[48] P. Axel, Phys. Rev. **126**, 671 (1962).
[49] M. Krtička and F. Bečvář, J. Phys. G: Nucl. Part. Phys. **35**, 014025 (2008).
[50] S. Péru and H. Goutte, Phys. Rev. C **77**, 044313 (2008).
[51] D. Gogny, in *Proceedings of the International Conference on Nuclear Physics, Munich, 1973*, edited by J. de Boer and H. J. Mang (North-Holland, Amsterdam, 1974), p. 48.
[52] J. Dechargé and D. Gogny, Phys. Rev. C **21**, 1568 (1980).
[53] J. Berger, M. Girod, and D. Gogny, Nucl. Phys. A **502**, 85 (1989).
[54] S. Péru and M. Martini, Eur. Phys. J. A **50**, 88 (2014).
[55] P. Sarriguren, A. Algora, and J. Pereira, Phys. Rev. C **89**, 034311 (2014).
[56] M. Martini, S. Péru, S. Hilaire, S. Goriely, and F. Lechaftois, Phys. Rev. C **94**, 014304 (2016).
[57] A. Koning, S. Hilaire, and S. Goriely, Nucl. Phys. A **810**, 13 (2008).
[58] S. Goriely, F. Tondeur, and J. Pearson, At. Data Nucl. Data Tables **77**, 311 (2001).
[59] S. Goriely, S. Hilaire, and A. J. Koning, Phys. Rev. C **78**, 064307 (2008).
[60] H. E. Johns, L. Katz, R. A. Douglas, and R. N. H. Haslam, Phys. Rev. **80**, 1062 (1950).
[61] P. Vesely, J. Kvasil, V. O. Nesterenko, W. Kleinig, P. G. Reinhard, and V. Y. Ponomarev, Phys. Rev. C **80**, 031302 (2009).